

1 **How do gravity waves triggered by a typhoon propagate from the**
2 **troposphere to the upper atmosphere?**

3 Qinzeng Li^{1,3}, Jiyao Xu^{1,2}, Hanli ~~Liu~~³Liu⁴, Xiao ~~Liu~~⁴Liu⁵, Wei Yuan^{1,3}

4 ¹State Key Laboratory of Space Weather, National Space Science Center, Chinese Academy of
5 Sciences, Beijing,100190, China,

6 ²School of Astronomy and Space Science, University of Chinese Academy of Science, Beijing,
7 100049, China,

8 ³Hainan National Field Science Observation and Research Observatory for Space Weather,

9 ³~~High~~⁴High Altitude Observatory, National Center for Atmospheric Research, Boulder, CO
10 80307-3000, USA,

11 ⁴~~School~~⁵School of Mathematics and Information Science, Henan Normal University, Xinxiang,
12 453007, China;

13

14 Correspondence to: xujy@nssc.ac.cn

15 **Abstract**

16 Gravity waves (GWs) strongly affect atmospheric dynamics and photochemistry and
17 the coupling between the troposphere, stratosphere, mesosphere, and thermosphere. In
18 addition, GWs generated by strong disturbances in the troposphere (e.g., thunderstorms and
19 typhoons) can affect the atmosphere of the Earth from the troposphere to the thermosphere.
20 However, the fundamental process of GW propagation from the troposphere to the
21 thermosphere is poorly understood because it is challenging to constrain this process using
22 observations. Moreover, GWs tend to dissipate rapidly in the thermosphere because the
23 molecular diffusion increases exponentially with height. In this study, a double-layer airglow
24 network was used to capture concentric GWs (CGWs) over China that were excited by the
25 Super Typhoon Chaba (2016). We used ERA-5 reanalysis data and Multi-functional
26 Transport Satellite-1R observations to quantitatively describe the propagation processes
27 ~~physical mechanism~~ of typhoon-generated CGWs from the troposphere, propagating
28 ~~throughout~~ the stratosphere , and mesosphere, ~~and to the~~ thermosphere. We found that the
29 CGWs in the mesopause region were generated directly by the typhoon in the troposphere.
30 However, ~~like the relay,~~ the backward ray tracing analysis suggested that CGWs in the
31 thermosphere originated from the secondary waves generated by the dissipation of the CGW
32 and/or nonlinear processes in the mesopause region.

33 1. Introduction

34 Gravity waves (GWs) can transfer momentum and energy from the lower to the
35 upper atmospheres, thereby affecting global circulation and the thermal and compositional
36 structures ~~and the distribution of chemical composition~~ in the middle and upper
37 atmospheres (Holton, 1983; Fritts and Alexander, 2003). Studies ~~on~~ of dynamical,
38 photochemical, and electrodynamics processes have indicated that GWs are fundamental
39 for the coupling process between the troposphere, stratosphere, mesosphere, and
40 thermosphere (Liu and Vadas, 2013; Smith et al., 2013; Vadas and Liu, 2013; Xu et al.,
41 2015; Vadas and Becker, 2019).

42 Concentric GWs (CGWs) are a unique type of GW and considered to be mainly
43 generated by convective activity in the troposphere. CGWs can also be generated by GW
44 ~~primary wave~~ breaking (Vadas and Becker, 2019; Lund et al., 2020; Kogure et al., 2020)
45 volcanoes (Duncombe, 2022), nuclear explosions (Pfeffer and Zarichny, 1962; Pierce et
46 al., 1971), and rockets (Liu et al., 2020). CGWs in the stratosphere and mesosphere
47 generated by thunderstorms have been widely reported since their sources are ubiquitous
48 (Taylor and Hapgood, 1988; Sentman et al., 2003; Suzuki et al., 2007; Yue et al., 2009;
49 Vadas et al., 2012; Xu et al., 2015; Heale et al., 2019; Smith et al., 2020). In addition, Liu
50 et al. (2014) utilized the Whole Atmosphere Community Climate model to study the
51 global CGWs. In previous studies, CGWs induced by typhoons were detected using
52 ground-based optical remote sensing (Suzuki et al., 2013) while those induced by
53 hurricanes and tropical cyclones were detected using the Suomi National Polar-orbiting
54 Partnership satellite (Yue et al., 2014; Xu et al., 2019) in the mesopause region.

55 Notably, GWs tend to dissipate rapidly in the upper atmosphere due to molecular
56 viscosity and thermal diffusion (Vadas, 2007). Thermosphere GWs that are not dissipated
57 can originate directly from the troposphere (Vadas, 2007; Azeem et al., 2015) or from
58 secondary GWs, which are generated from the breaking of primary GWs in the
59 mesosphere or thermosphere region (Vadas and Fritts, 2003; Vadas and Crowley, 2010;
60 Vadas and Azeem, 2021). Furthermore, Vadas and Becker (2019) for the first time
61 presented global simulations of tertiary CGWs from the dissipation of secondary CGWs
62 in the thermosphere. Moreover, wave-wave interaction, wave-mean flow interaction
63 (Franke and Robinson, 1999; Vadas and Fritts, 2001), self-acceleration, and nonlinear
64 breaking are other potential secondary wave generation mechanisms (Lund and Fritts,
65 2012; Fritts et al., 2015; Dong et al., 2020; Fritts et al., 2020; ~~Franke and Robinson, 1999;~~
66 Zhou et al. 2002; Heale et al. 2020). At the same time, tunneling has been deemed as a
67 mechanism that can couple waves from tropospheric sources to the thermosphere
68 (Walterscheid and Hecht, 2003; Gavrilov and Kshevetskii; 2018, Heale et al., 2021).
69 However, the lack of observations of the entire atmosphere limits our understanding of the
70 fundamental process of how GWs propagate from the lower ~~atmosphere~~ to the upper
71 atmosphere step by step on the aspect of observations.

72 This paper presents a case study examining CGWs excited by Super Typhoon
73 Chaba (2016). To this end, we utilized Multi-functional Transport Satellite-1R
74 (MTSAT-1R) observations, multi-layer European Centre for Medium-range Weather
75 Forecasts (ECMWF) ERA-5 reanalysis data (Hoffmann et al., 2019; Hersbach et al., 2020),
76 and high spatio-temporal resolution double-layer airglow network (DLAN) (Xu et al.,

77 2021) observations. The CGW observations from the troposphere to the stratosphere and
78 then to the mesosphere were taken from MTSAT-1R, ERA-5, and the DLAN. However,
79 given the observational limitations between the mesosphere and thermosphere, the two
80 layers are connected by ray tracing theory ~~the DLAN was utilized to identify the~~
81 ~~mesosphere and thermosphere via the ray tracing theory~~. The objectives of this study were
82 to (a) investigate ~~scrutinize~~ multi-layer CGW features produced by Super Typhoon Chaba
83 (2016) from near the ground to a height of 250 km, (b) to examine the entire propagation
84 process of the CGWs excited by typhoon from the lower atmosphere to the upper
85 atmosphere, and (c) to provide new insights into the coupling between different
86 atmospheric layers.

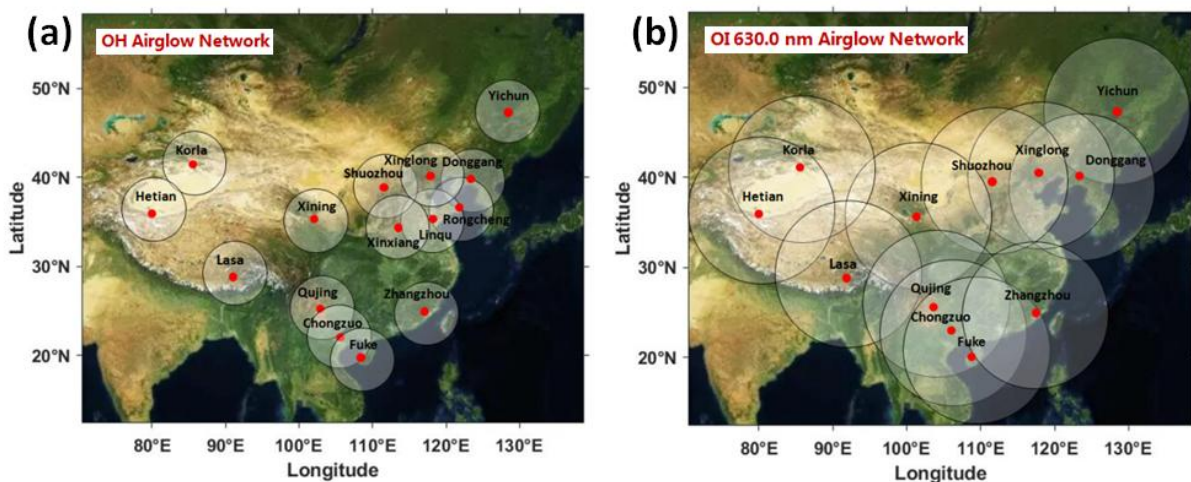
87 **2. Data and Methods**

88 **2.1 Double layer all-sky airglow imager network data**

89 A DLAN, including an OH layer (~87 km) and OI 630.0 nm layer (~250 km) was
90 established over mainland China. The research aim of the DLAN is to explore the
91 physical mechanism of vertical and horizontal propagation and the evolution of
92 atmospheric waves in the middle and upper atmosphere triggered by severe disasters, such
93 as typhoons, earthquakes, and tsunamis, ~~in various middle and upper atmospheric layers~~.
94 The OH airglow network comprises 15 stations, including the first no-gap OH airglow
95 all-sky imager network located in northern China (Xu et al., 2015). The OI 630.0 nm
96 airglow network contains 12 stations. Each imager consists of a 1024×1024 pixel
97 back-illuminated CCD detector and a Nikon 16 mm/2.8D fish-eye lens with a 180 ° field of
98 view (FOV). The OI 630.0 nm imager is operated at the 3.0 nm bandwidth filter with a

99 central wavelength of 630.0 nm. Observations using airglow optical remote sensing
 100 require only a few airglow imagers to cover a wide area although it is limited by
 101 meteorological conditions. Moreover, airglow observations can be used to monitor
 102 multi-layer GW activities. Figure 1a and 1b illustrate the OH and OI 630.0 nm network
 103 station distribution maps, respectively, in China. The OI 630.0 nm network covers nearly
 104 the entire mainland China. Furthermore, the DLAN provides an excellent solution for
 105 studying the coupling processes es ~~between~~ among different atmospheric layers, especially
 106 the mesosphere and thermosphere.

107 Several standard procedures were applied to raw airglow images, including star
 108 contamination subtraction, flat fielding to remove van Rhijin, and atmospheric extinction
 109 (Li et al., 2011). The GW structure was retrieved by taking the deviation of each
 110 processed image from a half-hour running average window image. Finally, the images
 111 were projected onto the Earth's surface using the standard star map software and the
 112 altitude of the airglow layer (Garcia et al., 1997). The altitudes of the OH and OI 630.0
 113 nm emission layers were set as approximately 87 km and 250 km, respectively.

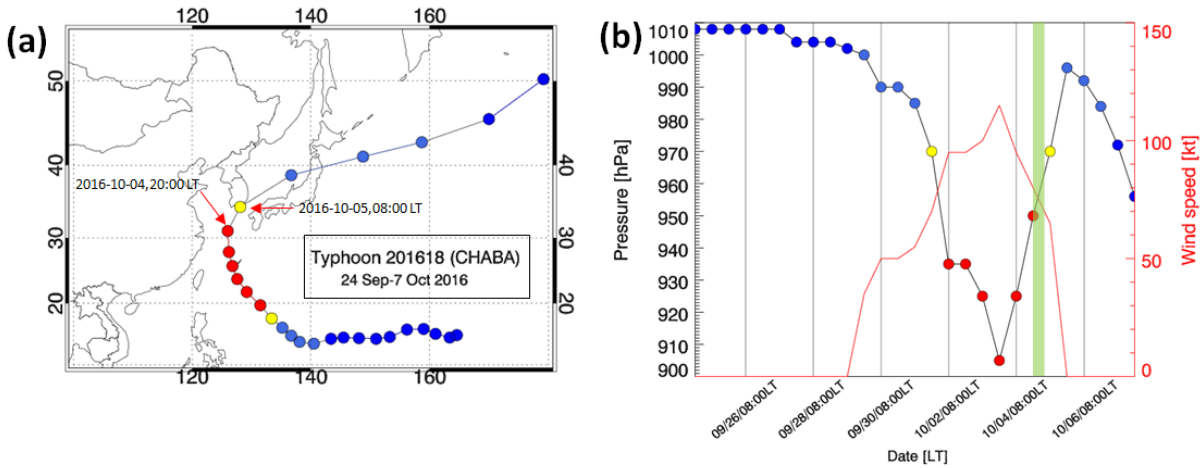


114 **Figure 1. (a)** OH airglow all-sky imager network (15 stations). **(b)** Red line (630 nm) airglow all-sky
 115 imager network (12 stations). The circles on the maps give the effective observation ranges of OH and
 116

117 Red line airglow imagers with diameters of about 800 km and 1800 km, respectively.

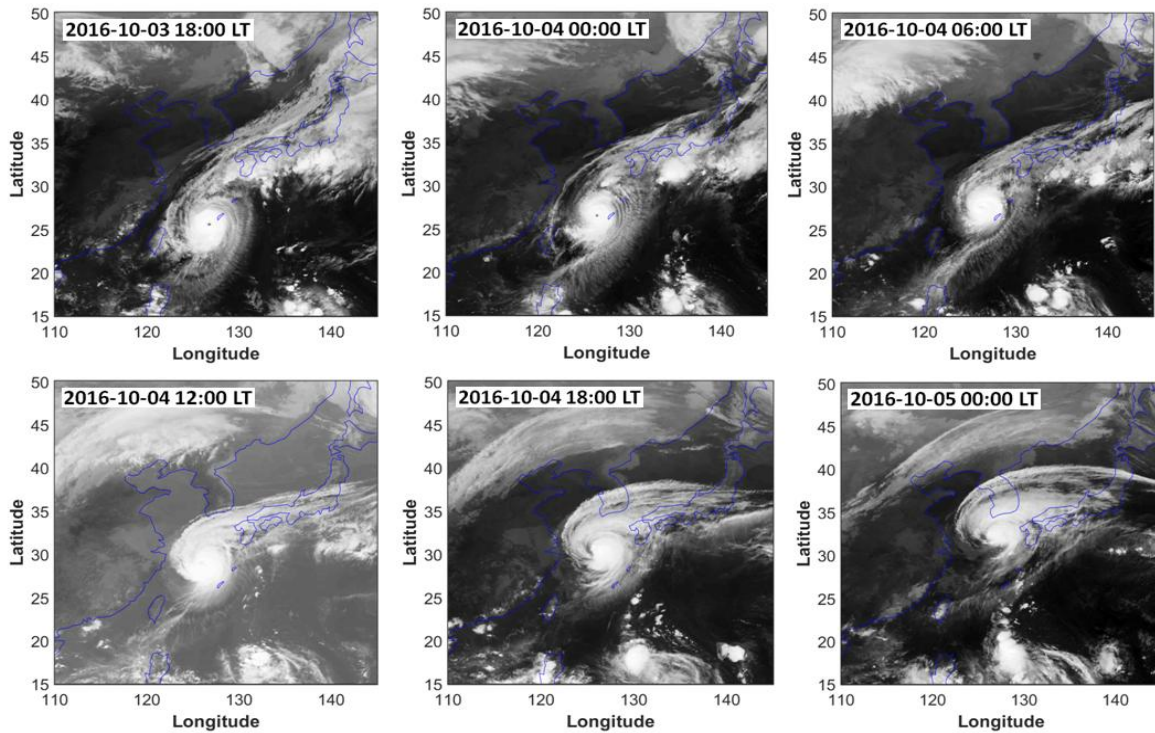
118 **2.2 Development of Super Typhoon Chaba**

119 Super Typhoon Chaba (2016) developed in the north-western Pacific on 24
120 September 2016 and its track is shown in Fig. 2a. Initially, it moved westward and then
121 turned north-westward on 30 September. The central pressure in the eye of the typhoon and
122 the maximum wind speed are shown in Fig. 2b. On 3 October 2016 at 20:00 LT, the
123 typhoon was in the mature stage with a minimum central pressure of 905 hPa and
124 maximum sustained winds of approximately 59 m/s. The typhoon moved northward on 4
125 October 2016 at 02:00 LT until 5 October 2016 at 02:00 LT. The typhoon continued
126 moving towards the northeast and disappeared on 8 October 2016 at 02:00 LT.
127 Consecutive satellite images of the typhoon from MTSAT-1R from 18:00 LT on 3 October
128 2016 to 00:00 LT on 5 October 2016 are shown in Fig. 3. MTSAT-1R, which belongs to the
129 Japan Meteorological Agency, comprises a series of Geo-stationary Meteorological
130 Satellites. MTSAT-1R is located at around 140 °E and covers East-Asia and the western
131 Pacific region. The MTSAT-1R consists of four infrared channels (IR1, IR2, IR3, and IR4)
132 and one visible channel (VIS). The MTSAT- IR1 was used in this study. The track of the
133 typhoon was beyond the effective FOV of the OH network and at the edge of the effective
134 FOV of the OI 630.0 nm network, ~~which provides an excellent example for observing the~~
135 ~~CGWs stimulated by the typhoon and studying the coupling among the atmospheric layers.~~



136

137 **Figure 2.** (a) The track of Typhoon Chaba is denoted by dots from 24 September to 7 October 2016
 138 every 12 hours. (b) Central pressure of Typhoon Chaba corresponding to the tracks in (a). The red line
 139 denotes the maximum sustained wind speed. The green shadow band denotes the time of
 140 ground-based airglow observation from 20:00 LT to 04:00 LT during the night of 4-5 October 2016.



141

142 **Figure 3.** Consecutive satellite images of the typhoon Chaba from MTSAT-1R. The period is from
 143 18:00 LT on 3 October 2016 to 00:00 LT on 5 October 2016, with an interval of 6 hours.

144 2.3 ERA-5 reanalysis data

145

ERA-5 is a fifth-generation ECMWF atmospheric reanalysis that provides hourly

146 data for many atmospheric and wave parameters. ERA-5 is produced using a
 147 four-dimensional variational data assimilation algorithm based on Integrated Forecast
 148 System (IFS), with 137 hybrid sigma/pressure (model) levels in the vertical from 1000 to
 149 0.01 hPa (0 to 80 km). More details of the model, data assimilation system, and
 150 observation data used to produce ERA-5 were described by Hersbach et al. (2020).
 151 Horizontal reanalysis temperature and wind data with a pre-interpolated resolution of 0.25°
 152 $\times 0.25^\circ$ and time resolution of 1 h were used in this study.

153 2.4 Ray tracing model

154 We used a ray-tracing method to estimate the source location of the thermospheric
 155 secondary CGWs. The model was based on a dispersion relation that considers molecular
 156 viscosity and thermal diffusivity (Vadas, 2007), as shown in Equation (1):

$$157 \quad m^2 = \frac{k_H^2 N^2}{\omega_r^2 (1 + \delta_+ + \delta^2 / Pr)} \left[1 + \frac{\nu^2}{4\omega_r^2} \left(k^2 - \frac{1}{4H^2} \right)^2 \frac{(1 - Pr^{-1})^2}{(1 + \delta_+ / 2)^2} \right]^{-1} - k_H^2 - \frac{1}{4H^2}, \quad (1)$$

158 where $\omega_r = \omega_r - (ku + lv)$ is the intrinsic frequency (ω_r is ground-based frequency);
 159 $\mathbf{k}^2 = k_H^2 + m^2$, $k_H^2 = k^2 + l^2$; H is the scale height; $\nu = \mu / \bar{\rho}$ is the kinematic viscosity where μ is
 160 the molecular viscosity and $\bar{\rho}$ is the background density; $\delta = \nu m / H \omega_r$, $\delta_+ = \delta (1 + Pr^{-1})$,
 161 where Pr is the Prandtl number. k , l , and m are the zonal, meridional, and vertical wave
 162 number components of the GW, respectively. The horizontal wavelength (k_H) of the
 163 CGW was obtained from the ground-based airglow observations;
 164 $N^2 = (g/T)(dT/dz + g/c_p)$ is the square of the Brunt-Väisälä frequency, where g is the
 165 gravitational acceleration, T is the background temperature, c_p is the specific heat at

166 constant pressure. The background temperature T and density $\bar{\rho}$ were obtained from the
 167 NRLMSISE-00 model (Picone et al., 2002).

168 The group velocity of the wave packet is formalized by Equation (2):

$$169 \quad c_{gi} = dx_i/dt = \partial\omega_{lr}/\partial k_i + V_i, \quad (2)$$

170 where $V_i(u, v, w)$ is the background wind, which was obtained from the Horizontal Wind
 171 Model 14 (Drob et al., 2015) and w is the vertical wind velocity, which was neglected. In
 172 this study, we assume that the background wind field is independent of time, so
 173 ground-based frequency ω_r remains constant along a ray's path (Lighthill, 1978).
 174 However, the actual wind field changes with time, which may lead to deviation between
 175 the ray tracing results and the wave source locations.

176 Using Equations (1)-(2), we yield the ground-based (zonal, meridional, and vertical)
 177 group velocity equation as follows (Vadas and Fritts, 2005):

$$178 \quad c_{gx} = \frac{k}{\omega_r B} \left[\frac{N^2(m^2 + 1/4H^2)}{(k^2 + 1/4H^2)^2} - \frac{v^2}{2}(1 - Pr^{-1})^2 \left(k^2 - \frac{1}{4H^2}\right) \frac{(1 + \delta_+ + \delta^2/Pr)}{(1 + \delta_+/2)^2} \right] + u, \quad (3)$$

$$179 \quad c_{gy} = \frac{l}{\omega_r B} \left[\frac{N^2(m^2 + 1/4H^2)}{(k^2 + 1/4H^2)^2} - \frac{v^2}{2}(1 - Pr^{-1})^2 \left(k^2 - \frac{1}{4H^2}\right) \frac{(1 + \delta_+ + \delta^2/Pr)}{(1 + \delta_+/2)^2} \right] + v, \quad (4)$$

$$180 \quad c_{gz} = \frac{1}{\omega_r B} \left\{ m \left[-\frac{k_H^2 N^2}{(k^2 + 1/4H^2)^2} - \frac{v^2}{2}(1 - Pr^{-1})^2 \left(k^2 - \frac{1}{4H^2}\right) \frac{(1 + \delta_+ + \delta^2/Pr)}{(1 + \delta_+/2)^2} \right. \right. \\ \left. \left. + \frac{v^4(1 - Pr^{-1})^4}{16H^2\omega_r^2} \frac{(k^2 - 1/4H^2)^2}{(1 + \delta_+/2)^3} - \frac{v^2}{Pr H^2} \right] - \frac{v_+ \omega_r}{2H} \right\}, \quad (5)$$

$$181 \quad \text{where } B = \left[1 + \frac{\delta_+}{2} + \frac{\delta^2 v^2}{16\omega_r^2} (1 - Pr^{-1})^4 \frac{(k^2 - 1/4H^2)^2}{(1 + \delta_+/2)^3} \right], \nu_+ = \nu(1 + Pr^{-1}).$$

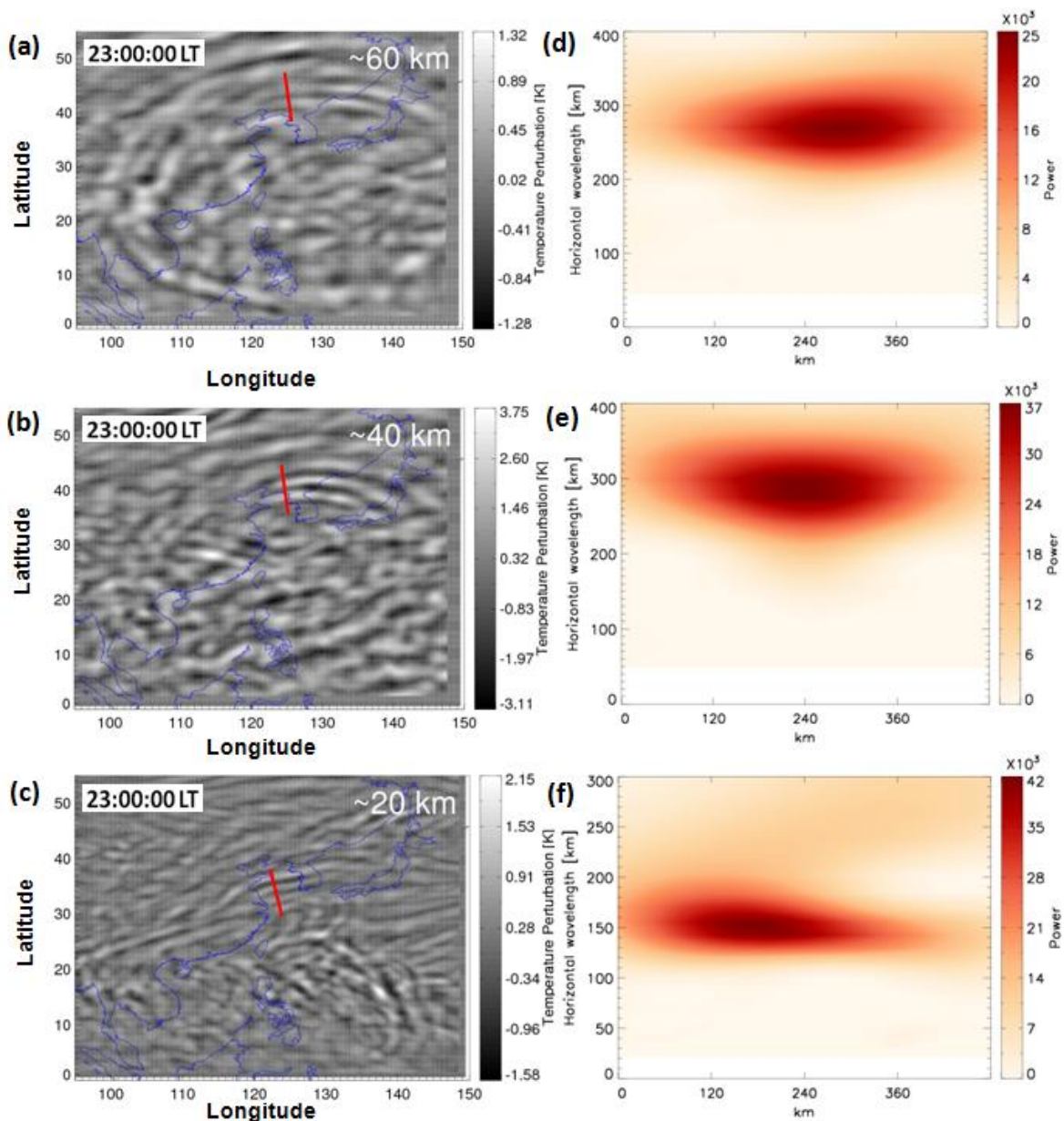
182

183 3. Results

184 3.1 Propagation of typhoon-induced CGWs in the stratosphere

185 We extracted the ~~stratospheric CGW~~CGWs excited by ~~the Typhoon typhoon in the~~
186 ~~stratosphere~~ from ~~the~~ERA-5 reanalysis ~~data~~. Figure 4a, 4b, and 4c show the multilayer
187 temperature perturbations at approximately 60 km, 40 km, and 20 km at 23:00 LT,
188 retrieved from the ERA-5 reanalysis on 4 October 2016, respectively. Temperature
189 perturbations were calculated by subtracting the background with a 7×7 grid point running
190 mean at 20 km and 17×17 grid point running mean at 40 km and 60 km. We found that
191 the temperature disturbance was about ± 1.5 -2 K at 20 km and ± 3 -4 K at 40 km. Using
192 the ECMWF reanalysis data, Kim et al. (2009) reported a similar temperature
193 disturbance(± 4 K) at 40 km altitude. Becker et al. (2022) showed that typical
194 temperature perturbation amplitudes simulated by a High Altitude Mechanistic general
195 Circulation Model were ± 1 -2 K in the wintertime lower stratosphere and ± 5 K in the
196 stratopause region. However, the temperature disturbance at 60 km ~~in ERA-5 altitude~~ was
197 only ± 1.3 K and did not increase with increasing altitude, which may be caused by this
198 altitude being well within the sponge layer of the reanalysis model. Figure 4d, 4e, and 4f
199 show the corresponding wavelet analysis contours of the red line in Fig. 4a, 4b, and 4c.
200 The expansion area of CGW at the height of 20 km (Fig. 4c) was small, and the horizontal
201 wavelength was approximately 150 km from Fig. 4f. ~~Liu et al. (2014) utilized the Whole~~
202 ~~Atmosphere Community Climate model and showed that the horizontal area of the CGW~~
203 ~~expansion increases with increasing altitude.~~The CGWs were present over a large area of
204 0°N - 50°N and 100°E - 150°E at approximately 60 km. The distance of the CGWs,
205 extending from the center of the circle ranged from 500 km (at approximately 20 km

206 height) to 3000 km (at approximately 60 km height), which suggests that the larger-scale
 207 CGW arrive earlier at higher altitudes (have faster vertical group velocities) than the
 208 smaller-scale waves (Vadas and Azeem, 2021). The ERA-5 reanalysis data was utilized
 209 for characterizing the scale of the CGWs and indicated no small-scale fluctuation.
 210 According to the wavelet analysis of Fig. 4d and 4e, the horizontal wavelengths of the
 211 northward propagating CGW at 60 km (Fig. 4a) and 40 km (Fig. 4b) were approximately
 212 265 km and 290 km, respectively.



213

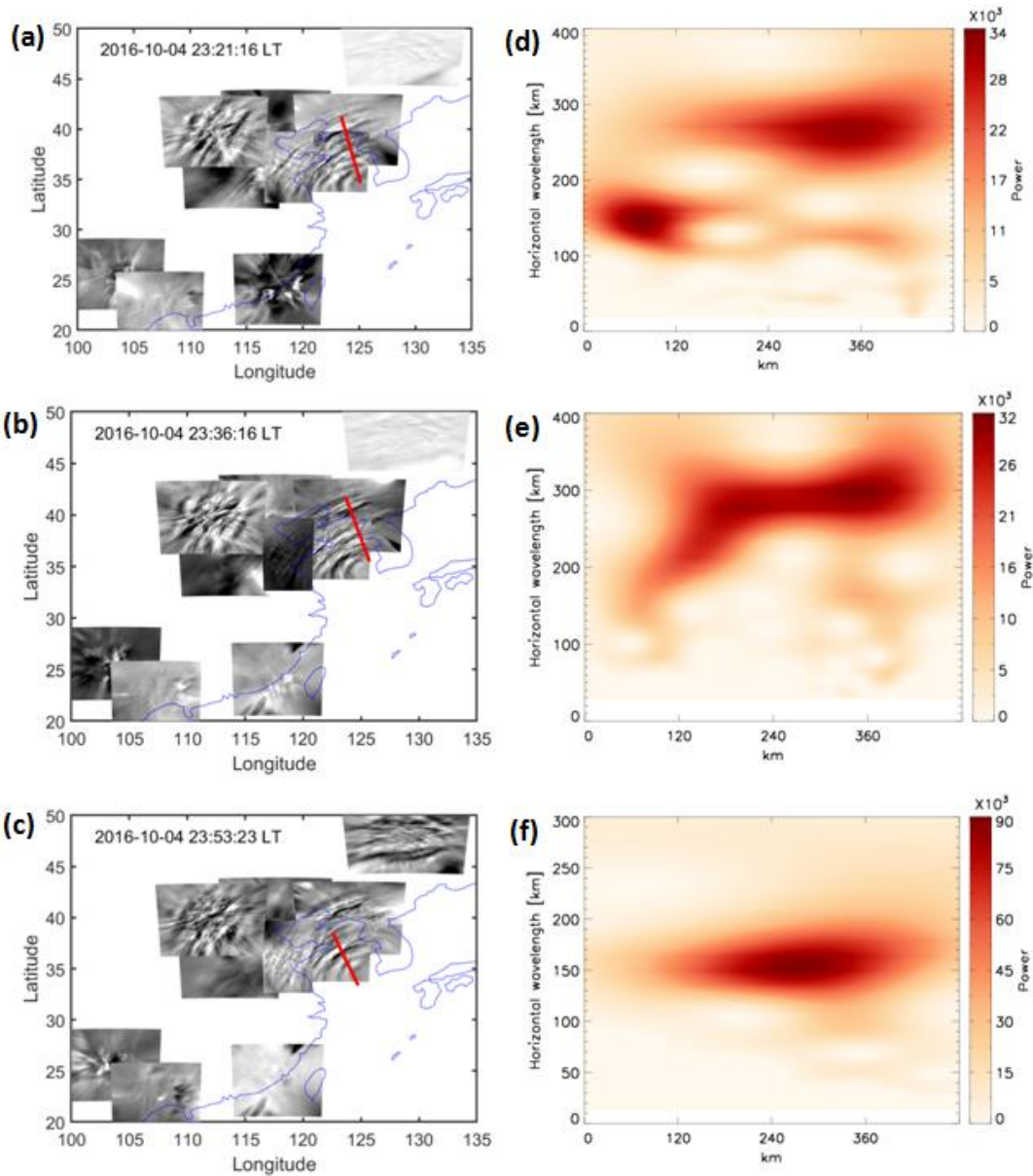
214 **Figure 4.** Temperature perturbations at (a) ~60 km , (b) ~40 km, and (c)~20 km at 23:00 LT on 4
215 October 2016 derived from ERA-5 reanalysis. (d) Wavelet power spectrum along the red line in (a), (e)
216 wavelet power spectrum along the red line in (b), and (f) wavelet power spectrum along the red line in
217 (c).

218 3.2 Propagation of typhoon-induced CGWs in the mesosphere

219 As the typhoon moved along the coast of China, CGWs were identified at ten
220 stations in the OH network. Animation 1 shows that CGWs were observed by the OH
221 airglow network during 20:00–04:00 LT (the detailed data can be downloaded from the
222 Supplementary Material). As the weather conditions in North China during the study
223 period were better than those in South China, we identified clearer wave structures at the
224 northern stations than at the southern stations. Nevertheless, circular wave structures
225 were visible for brief clear weather intervals at the Zhangzhou, Qujing, and Chongzuo
226 stations. The CGWs in the mesopause region extended to 2500 km, thereby nearly
227 covering the effective FOV of the OH airglow network.

228 As long as the CGWs do not encounter the critical layer or break, the ~~phase plane of~~
229 CGWs ~~generated in the lower atmosphere from ERA-5 reanalysis datasets~~ can propagate
230 to the OH airglow layer. Through the propagation group velocity, we can determine the
231 propagation time to the OH layer. A single dominant horizontal wavelength is seen at
232 ~~each the~~ altitudes of 20 km, 40 km, and 60 km in the ERA-5 reanalysis ~~due to the limited~~
233 ~~resolution~~. In contrast, the horizontal scales of the CGW obtained by the OH airglow
234 network were diverse, ranging from approximately 30 km to 300 km ~~as the imager has~~
235 ~~much higher spatial resolution~~. More importantly, we found some CGWs in the OH
236 airglow layer, which were close to the CGW wavelengths at 20 km, 40 km, and 60 km

237 altitudes. To verify whether ~~the phase plane of~~ the same wave was propagated from the
238 reanalysis data layer to the OH layer, we used the group velocity to estimate the time
239 when the ~~phase plane of~~ CGW at the altitudes of 20 km, 40 km, and 60 km reached the
240 OH airglow layer. The times required for the CGW in the three-layer disturbance diagram
241 in Fig. 4a, 4b, and 4c to reach the OH layer were approximately 21 minutes, 36 minutes,
242 and 53 minutes. Therefore, the times when the CGWs visible in phase plane of CGWs
243 ~~from~~ ERA-5 at ~~the height of~~ 60 km, 40 km, and 20 km would reaches the OH airglow
244 layer ~~is are~~ approximately 23:21 LT, 23:36 LT, and 23:53 LT as shown in Fig. 5a, 5b, and
245 5c, respectively. The wavelet analysis of Fig. 5f showed that the horizontal wavelength
246 of CGW in the OH airglow layer (Fig. 5c) is approximately 156 km, the observed
247 period is approximately 23 min, and the horizontal speed is approximately 113 m/s,
248 which is similar to the dominant horizontal wavelength of the CGWs in the ERA-5
249 reanalysis at 20 km altitude. Similarly, the horizontal wavelengths of CGW in the OH
250 airglow layers (Fig. 5a and 5b) were approximately 270 km and 295 km from the wavelet
251 analysis of Fig. 5d and 5e, which is similar to the dominant horizontal wavelength of the
252 CGWs in the ERA-5 reanalysis at 60 km and 40 km altitudes. This suggests that the same
253 CGW event can be perfectly tracked over different altitudes and that the CGWs in the
254 mesosphere propagated upward from the stratosphere at different layer altitudes and that
255 ~~the CGWs in the mesosphere come from the direct excitation of the typhoon.~~



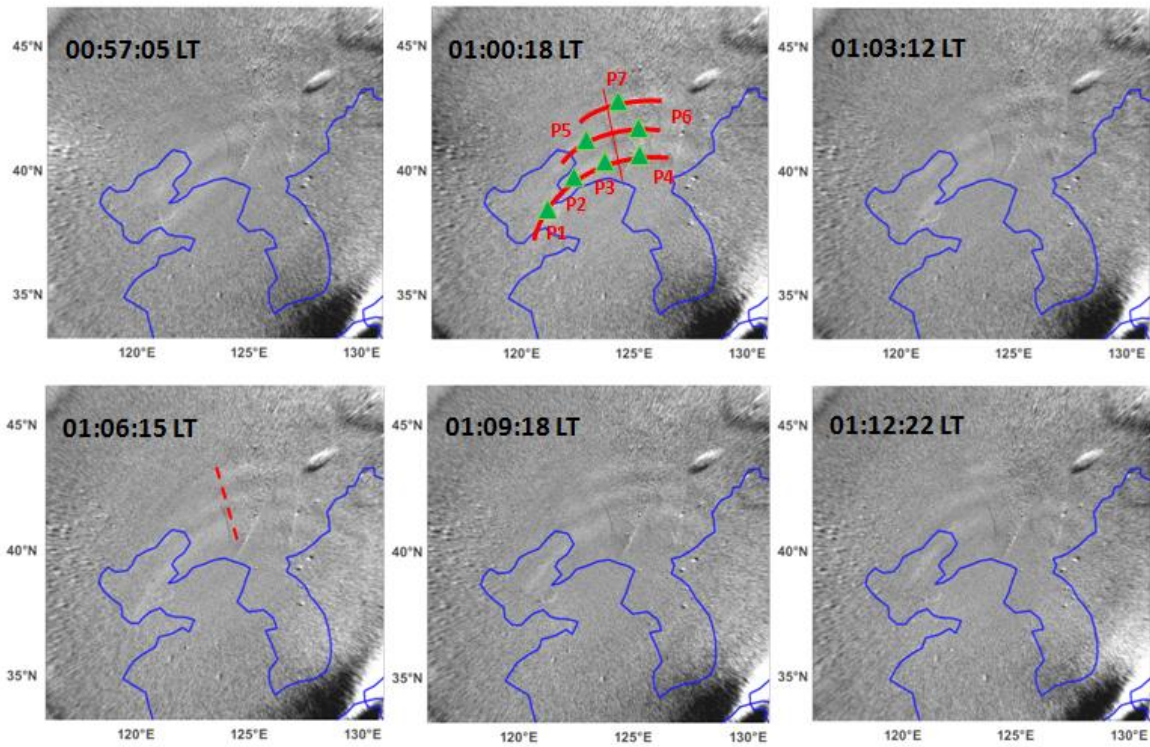
256

257 **Figure 5.** OH airglow emission perturbations induced by CGWs observed by the OH airglow imager
 258 network at (a) 23:21 LT, (b) 23:36 LT, and (c) 23:53 LT on 4 October 2016. (d) Wavelet power
 259 spectrum along the red line in (a), (e) wavelet power spectrum along the red line in (b), and (f)
 260 wavelet power spectrum along the red line in (c).

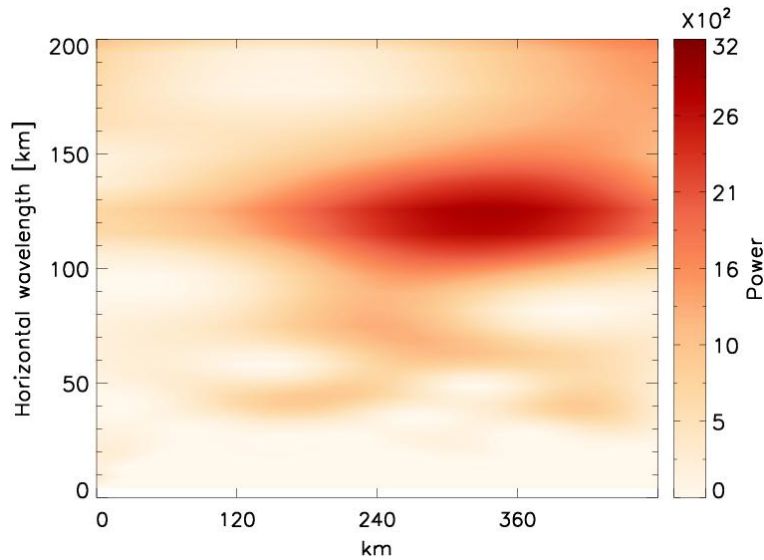
261 3.3 How typhoon-induced CGWs propagate to the thermosphere

262 Figure 6 shows the time sequence of the OI 630.0 nm airglow images from 00:57:05
 263 LT to 01:12:22 LT on the night of 4 October 2016. Three curved phase fronts are clearly
 264 visible. The wave packet observed in the OI 630 nm airglow was quasi-monochromatic.

265 According to the wavelet analysis spectrum in Fig. 7, the horizontal wavelength was
266 approximately 120 km. The observed wave observation-period and phase velocity were
267 10 min and 200 m/s, respectively. The horizontal wavelength was somewhat less than the
268 ~~multi-scale~~-typhoon-induced concentric traveling ionosphere disturbances with a
269 horizontal wavelength from 160 to 200 km in the GNSS-TEC network as reported by
270 Chou et al. (2017). The CGW observed in the OI 630.0 nm airglow had much faster phase
271 speed and shorter period than that observed in the mesosphere, which indicate that its
272 propagation trajectory was relatively vertical. This means that they will not propagate as
273 far horizontally as the CGWs noted as dominant in the OH layer. Indeed, compared with
274 the long-distance extension of the CGWs in the mesosphere, the horizontal propagation
275 distance of the CGWs in the thermosphere was only 600 km from OI 630.0 nm network
276 observation. ~~Numerical simulations revealed that the thermosphere GWs may originate~~
277 ~~from secondary GWs generated by the breaking of primary GWs in the mesosphere or~~
278 ~~thermosphere region (Vadas and Crowley, 2010).~~ Vadas and Crowley (2010) showed that
279 thermospheric GWs may be secondary GWs generated by the breaking of primary GWs
280 in the mesosphere and thermosphere. We argue that ~~the following phenomenon can~~
281 ~~represent the potential driver of this pattern.~~ ~~Specifically,~~ the thermospheric CGW
282 observed by the OI 630.0 nm airglow imager was not directly generated by the typhoon,
283 but a secondary GW. To test this hypothesis, backward ray-tracing analysis was applied.
284 In this way, we determined the source of the CGW observed in the thermosphere.



285
 286 **Figure 6.** Time sequence of OI 630.0 nm airglow emission perturbation images observed by Donggong
 287 station during 00:57:05 – 01:12:22 LT on the night of 4 October 2016. Green triangles (P1-P7) in the
 288 red arcs are used as ray tracing sampling points. The blue line in each panel represents the coastline.

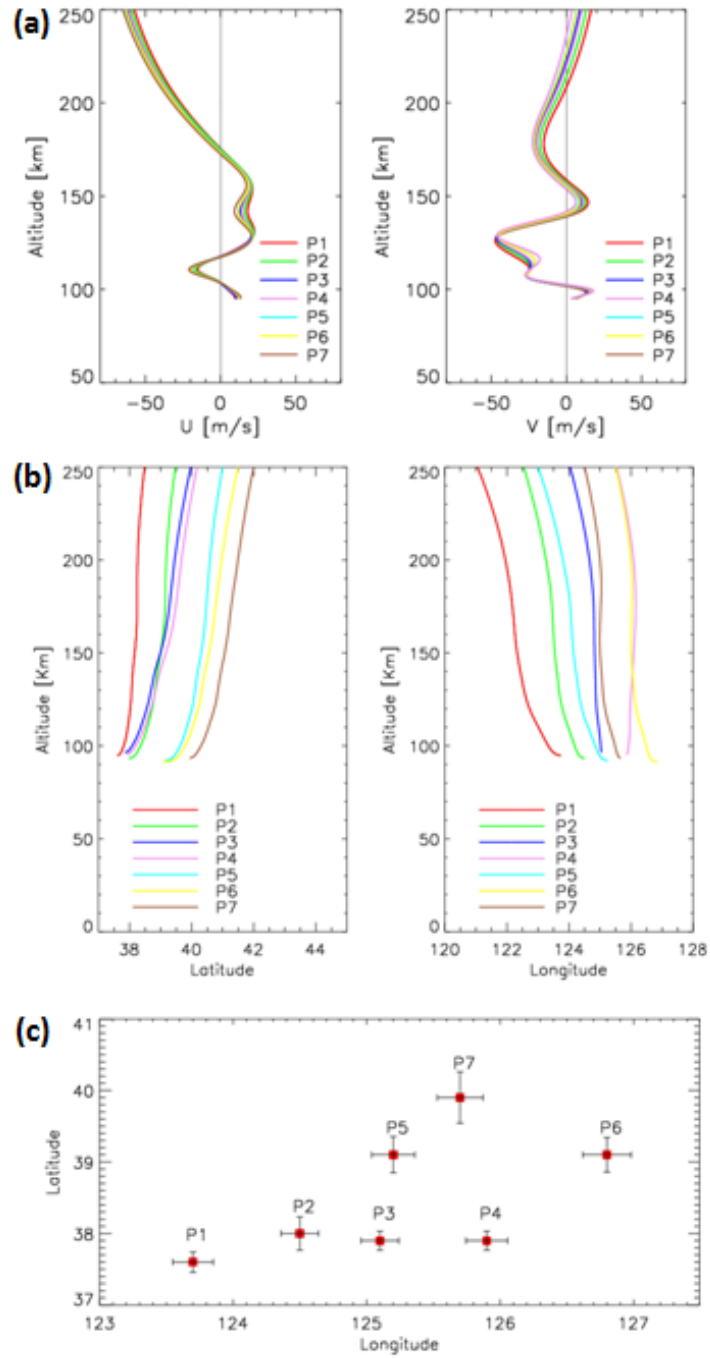


289
 290 **Figure 7.** Wavelet power spectrum along the red line at 01:00:18 LT in Fig. 6.
 291 We sampled seven points (green triangles) on a circular wavefront (red line in Fig. 6) at
 292 01:00:18 LT as the starting point for backward ray tracing. The starting height of the

293 backward ray tracing was 250 km. The profile of the winds used in the ray tracing is
294 shown in Fig. 8a. The ray tracing trajectories of the seven sampling points are shown in
295 Fig. 8b. We used the following criterion to terminate the ray tracing: the square of the
296 vertical wavenumber should be negative. We started the ray-tracing at heights of 240 km,
297 250 km, and 260 km , and analyzed the results~~The ray tracing results of three different~~
298 ~~heights of 240 km, 250 km, and 260 km were analyzed.~~ The maximum uncertainty of
299 horizontal change of ray-tracing termination point caused by different starting heights
300 was approximately $\pm 0.36^\circ$ in latitude and $\pm 0.17^\circ$ in longitude (see Figure 8c).
301 Subsequently, seven backward traced trajectories took 37 minutes and terminated at an
302 altitude of approximately 95 km thereby indicating that a reflection layer was
303 encountered. According to linear theory, this~~it met the reflection layer ,which, according~~
304 ~~to linear theory,~~suggests that the thermospheric CGW could not have come from below
305 95 km. ~~according to linear theory.~~The thermospheric ~~CGW~~ could~~must~~ have been
306 generated at any altitude between 95 km and the altitude of the OI 630.0 nm airglow. In
307 other words, the CGW observed in the thermosphere was excited after approximately
308 00:23 LT. ~~Meanwhile,~~Figure 9 presents the CGWs observed by the OH airglow network
309 at 00:23:22 LT. We superimposed the thermospheric CGWs along with the starting ray
310 tracing points (green triangles) reproduced from Fig. 6, and the backward ray tracing
311 termination points (red diamonds) on the OH airglow observation images. The dotted
312 circle represents the approximate fitting thermospheric CGW fronts. The center of the
313 circle is marked by a blue cross. Compared with the single-scale wave observed in the OI
314 630.0 nm layer, multi-scale CGWs were visible from OH network observations. We

315 found that the termination points of ray tracing almost fell above the mesopause region,
316 ~~which showing clear signs of dissipation and/or nonlinear processes~~. This suggests that
317 the CGW observed in the thermosphere did not directly originate from the typhoon but
318 may have emerged due to the dissipation and/or nonlinear processes of typhoon-induced
319 CGW in the mesopause region. However, the backward tracing terminal positions (red
320 diamonds in Fig. 9) did not coincide with the fitting circle center position (blue cross in
321 Fig. 9). Nevertheless, according to numerical simulation work by Vadas et al. (2009),
322 large winds can shift the apparent center of concentric rings from the location of the
323 convective plume. Indeed, we found strong southward winds from 100 km to 140 km
324 (with a peak value of 50 m/s at 150 km altitude) and from 160 km to 220 km (with a peak
325 value of 25 m/s at 175 km altitude) altitudes (right panel of Figure 8a). So the center of
326 the thermospheric CGW can be shifted southward from the location of the thermospheric
327 CGW sources in the mesopause region. For the zonal wind, the westward wind
328 dominated from the upper mesosphere to the thermosphere (left panel of Figure 8a).
329 Similarly, the thermospheric CGW center position shifted westward. Therefore, the
330 assumed center (blue cross) of the partial concentric ring GWs (blue arcs) actually shifted
331 to the southwest from the real source location—, which ~~can~~ may explain why the
332 ray-tracing result for the assumed GW source did not match the fitting center of the
333 partial concentric ring thermospheric GWs. Another possible mechanism is that the wave
334 phase speeds are accelerated by accelerating background winds. As mentioned above, the
335 ground-based frequency ω_r remains constant along a ray's path assuming the background
336 wind field is independent of time (Lighthill, 1978). However, transient effect (time

337 derivatives of the background wind components giving rise to time derivative of the
338 frequency for a particular ray) may cause the phase speeds to be accelerated, which may
339 lead to the ray-tracing results did not match the real locations. As the ray-tracing model
340 used in this study depended on the linear theory and did not consider the wave-wave and
341 wave-mean flow interactions and tunneling, the ray tracing results were limited and
342 should be taken into consideration carefully.



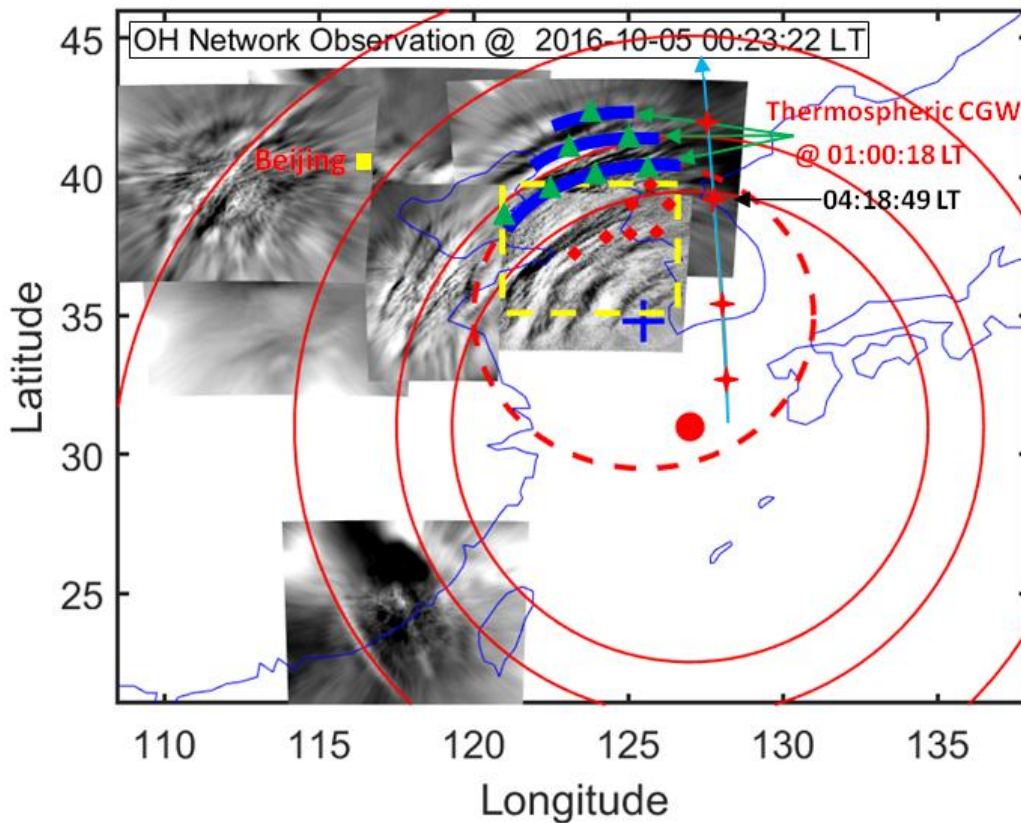
343

344 **Figure 8.** (a) Wind profiles along the seven ray-tracing paths. (b) Ray paths of the wave starting from

345 the seven sampling points in Fig.6. (c) Horizontal area distribution of the terminal positions of the

346 seven backward traced trajectories. Error bars give standard deviation for each point from the starting

347 altitude of 240 km, 250 km, and 260 km.



348

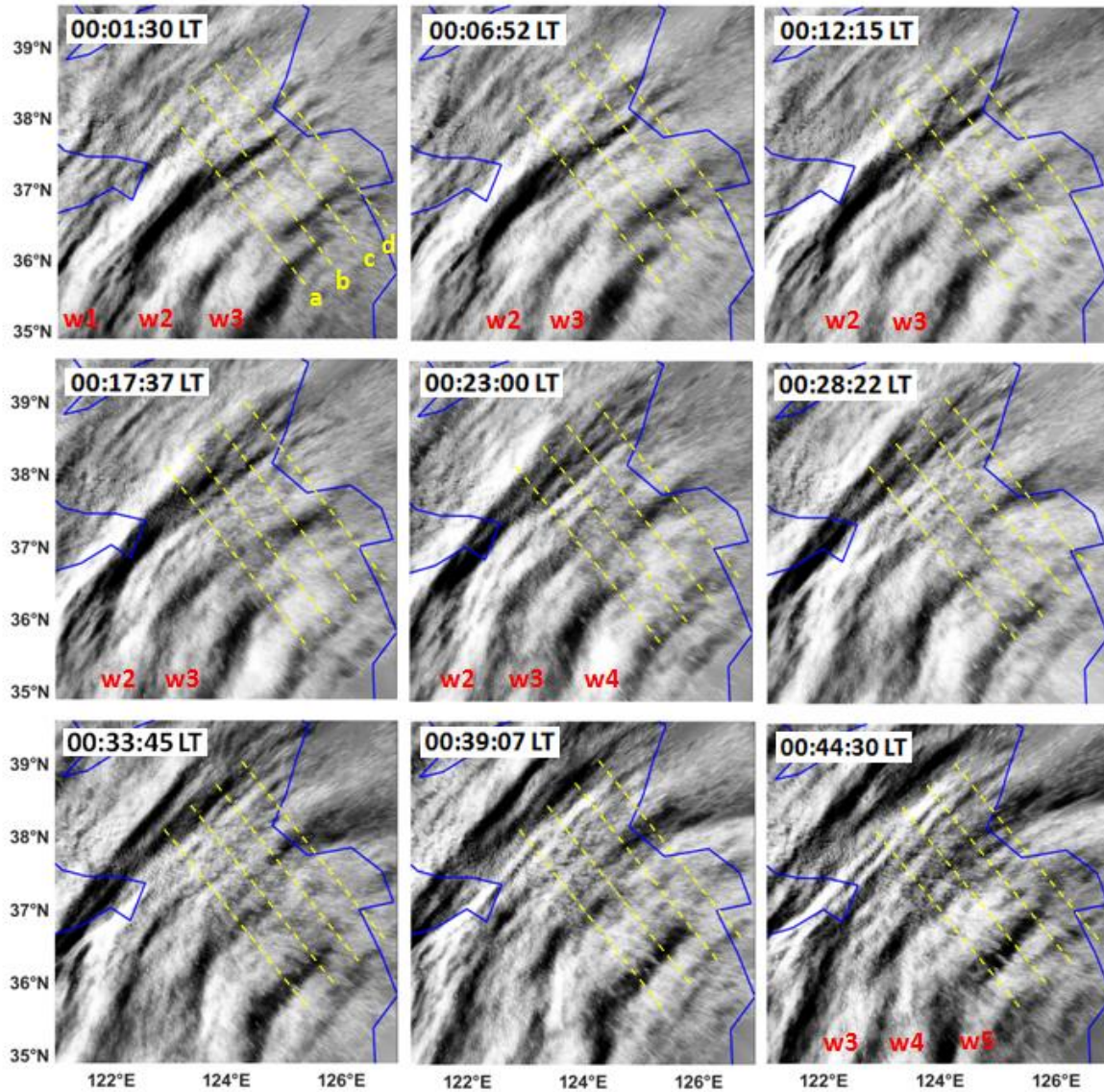
349 **Figure 9.** Double layer CGW superimposed graph: The blue arcs represent the thermospheric CGW
 350 observed at 01:00:18 LT. The dotted circle represents the approximate fitting blue arcs. The blue cross
 351 marks the center of the circle. The solid circles represent the approximate fitting CGWs observed by
 352 the OH airglow network. The red dot marks the center of the circles. The green triangles and red
 353 diamonds represent the trace start and termination points, respectively. The red crosses represent the
 354 sounding footprints of the TIMED/SABER measurements. The yellow box marks the location of the
 355 meteor radar station.

356

357 **4. Discussion**

358 Figure 10 presents a time sequence of OH airglow images in the range marked by
 359 the yellow dotted rectangle in Fig. 9. The images were retrieved from the Rongcheng
 360 station from 00:01:30 to 00:44:30 LT on the night of 4 October 2016. At 00:01:30 LT,
 361 three distinct curved wavefronts with horizontal wavelengths of approximately 96 km

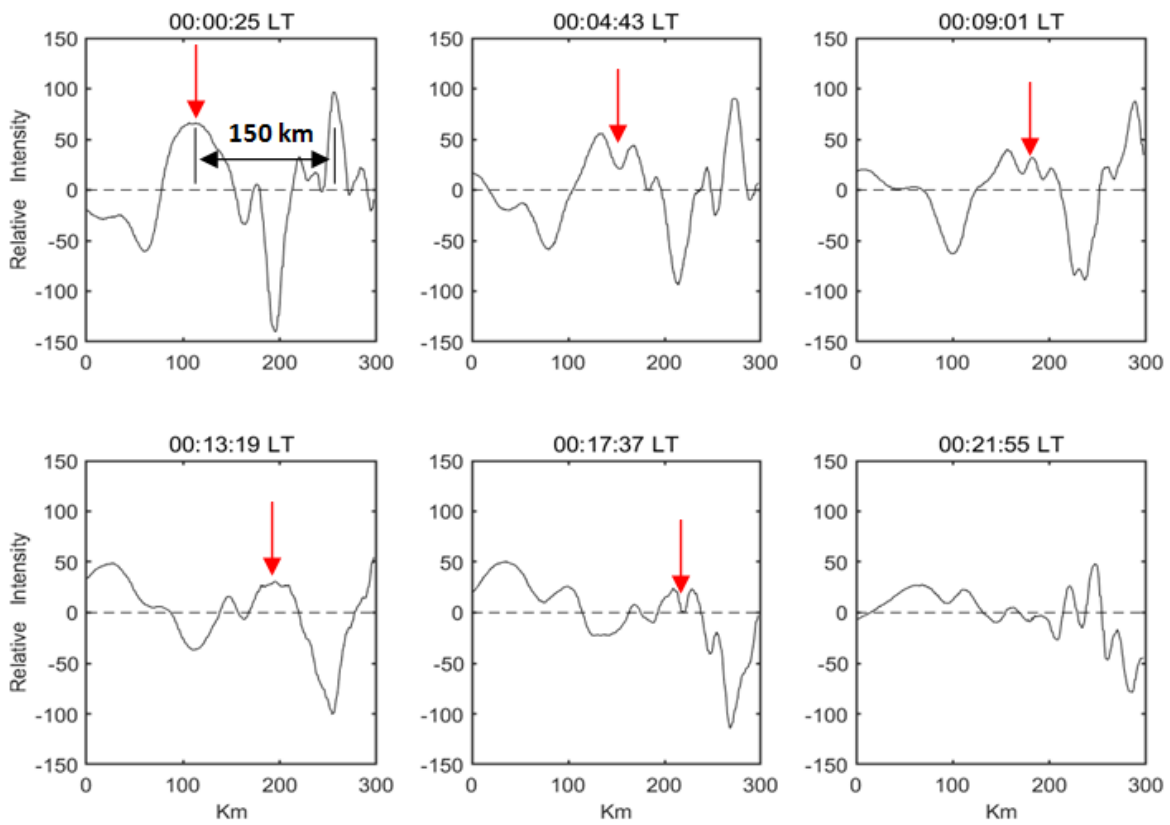
362 were identified. Interestingly, wavefronts 2 and 3 collided and connected in the northeast,
 363 indicating that wave-wave nonlinear interactions may have occurred.



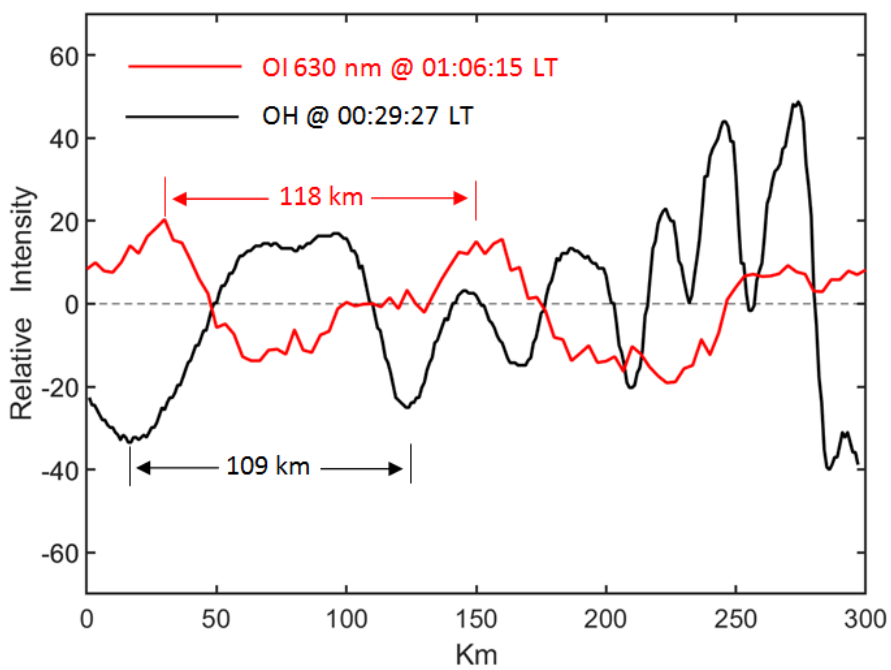
364
 365 **Figure 10.** Time sequence of OH airglow emission perturbation images observed by Rongcheng
 366 station during 01:01:30-00:44:30 LT on the night of 4 October 2016. w1-w5 denote the wavefronts of
 367 the CGW. The blue line in each panel represents the coastline.

368 ~~We elucidated the dissipation process of the CGWs in detail by examining the~~
 369 ~~evolution process of their amplitude.~~ Figure 11 shows the time series of the OH image
 370 slices perpendicular to the wavefronts (w1-w5). A dominant wavelength of approximately

371 150 km can be confirmed at 00:00:25 LT. ~~As a result, we~~ We found a significant
372 attenuation of the amplitude from 00:~~0600:52-25~~ LT to 00:17:37 LT. At 00:~~0600:52-25~~ LT,
373 while the relative average power was 2.3×10^3 , and the amplitude decreased gradually
374 with time. At 00:17:37 LT, the average power decreased to 0.15×10^3 . We also identified
375 the generation of approximately 110 km and 20-50 km small-scale waves from the larger
376 scales, which may be caused by wave-wave nonlinear interactions and/or wave breaking.
377 We overlaid the OI 630 nm airglow relative intensity variation on the OH airglow
378 variation and Figure 12 shows OH and OI 630 nm airglow relative intensity variations.
379 The OH plot was obtained at 00:29:27 LT and the OI 630 nm plot at 01:06:15 LT. The
380 time interval of 37 min was calculated by the above ray tracing analysis. We obtained
381 similar scale fluctuations were obtained in the two airglow layers. The horizontal
382 wavelength of the wave obtained by the OI 630 nm airglow layer was approximately 118
383 km. The OH airglow layer has also obtained near-scale fluctuations with wavelengths of
384 approximately 109 km. These waves could be the same waves seen in the thermosphere.
385 Therefore, the CGW in the thermosphere may come from breaking or nonlinear processes
386 of that primary gravity waves.



387
 388 **Figure 11.** Time series of averaged OH image slices perpendicular to the wavefronts as marked by
 389 four yellow dotted lines (a, b, c, and d) in Fig.10. The wavefronts propagate from left to right. The red
 390 arrows mark the evolution of the wavefront peak.



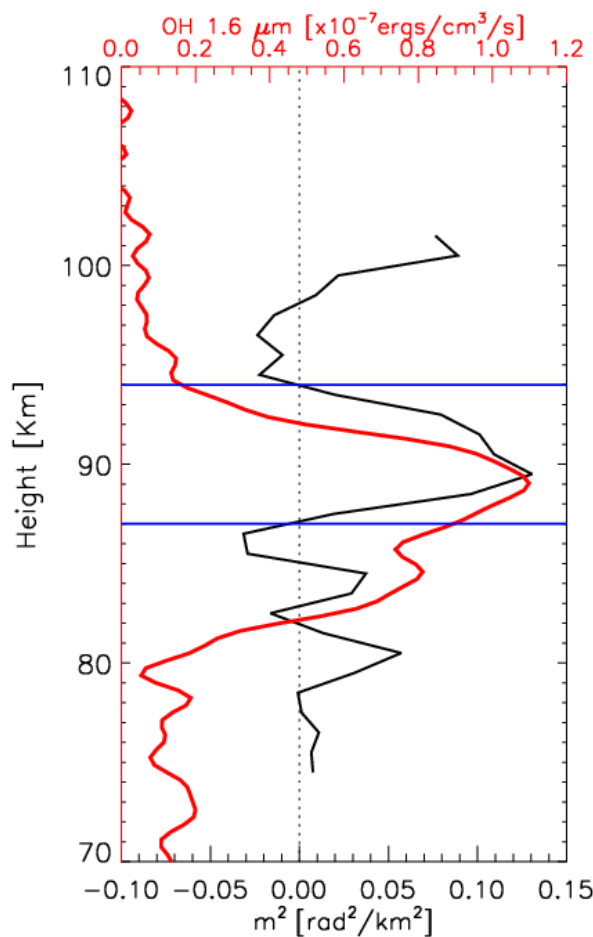
391

392 **Figure 12.** OH (black) and OI 630 nm (red) airglow relative intensity variations. The OH relative
393 intensity variation is obtained as in Fig. 11. The OI 630 nm relative intensity variation is from the red
394 dotted line in Fig.10 at 01:06:15 LT.

395 Note that wave ~~However, wavepacket~~ amplitude fluctuations can also result from the
396 transient nature of the wavepacket. The propagation state can be studied by using the
397 dispersion relationship with GW. However, but the dissipation region of the CGW lacks
398 the real-time background temperature and wind field. In this context, the limb-viewing of
399 Sounding of the Atmosphere using Broadband Emission Radiometry (SABER)
400 instrument on the Thermosphere Ionosphere Mesosphere Energetics and Dynamics
401 (TIMED) satellite ~~TIMED/SABER~~ can be beneficial because it occurred near the
402 wave-dissipation region; however, the time lag was close to approximately 4 h. ~~On this~~
403 ~~basis, we used the meteor radar~~ Background wind field data were obtained from an
404 ATRAD MDR6 all-sky VHF meteor radar at ~~from the~~ Beijing station ~~as auxiliary~~
405 ~~information~~. We further examined the dispersion relationship of GW, thereby shedding
406 some light on the possible propagation state of dissipative waves. Figure 13 presents the
407 vertical wave number m^2 profile derived from the Beijing meteor radar wind and the
408 temperature from the SABER ~~TIMED/SABER~~ TIMED measurement location ~~sound~~ at
409 04:18:49 LT, as marked in Fig. 9. The wave parameters used were from the wavefronts
410 (w1-w5) in Fig.10. The average horizontal wavelength was approximately 96 km and the
411 average observed phase velocity is approximately 90 m/s. We identified a clear duct
412 (from 87 km to 94 km) near the peak of the OH airglow layer. Note that the duct can
413 control the horizontal propagation of CGW. This implies that the CGW may indeed be
414 dissipated. In contrast, the upper boundary of the duct coincided with the height of the

415 ray-tracing termination area mentioned above. During wave dissipation, momentum
 416 deposition occurs in the background atmosphere and can produce bodyforces that
 417 stimulate secondary GWs (Fritts et al., 2006; Chun and Kim, 2008; Smith et al., 2013;
 418 Vadas et al., 2018; Heale et al., 2020). In addition, secondary waves can be generated by
 419 momentum transferred nonlinearly from the primary wave mode to harmonics or
 420 subharmonics (Snively, 2017). Local momentum flux divergence associated with wave
 421 breaking, vortex generation, and wave interactions can also generate secondary GWs
 422 (Fritts et al., 2006).

423



424

425 **Figure 13.** Vertical wave number m^2 profile (black) derived from the temperature from
 426 TIMED/SABER measurement locations at 04:18:49 LT and the meteor radar wind from Beijing
 427 station marked in Fig. 9. The red line represents the OH1.6 μm emission intensity obtained by the

428 | TIMED/SABER. The horizontal blue lines represent the top and bottom boundaries of the duct region.

429

430 **5. Summary**

431 In this study, a DLAN was used to capture CGWs over China that were excited by
432 the Super Typhoon Chaba (2016). As Super Typhoon Chaba (2016) moved northward
433 along the coast of the Chinese Mainland and developed to a mature stage, remarkable
434 multi-layer CGW features produced by the Typhoon from near the ground to a height of
435 250 km were observed by ERA-5 reanalysis and airglow network. We applied the
436 MTSAT-1R observations, ERA-5 reanalysis data, and backward ray tracing to
437 quantitatively describe the physical mechanism of typhoon-generated CGWs propagating
438 throughout the stratosphere, mesosphere, and thermosphere.

439 The temperature disturbance was approximately $\pm 1.5\text{-}2$ K at 20 km and $\pm 3\text{-}4$ K at
440 40 km. However, the temperature disturbance (± 1.3 K) at 60 km altitude did not increase
441 with further increase in altitude, which may be caused by the sponge layer effect. Using
442 reanalysis of multi-layer temperature disturbance, group velocity of gravity wave and
443 wavelet analysis, we demonstrated that the CGWs in the mesopause region were excited
444 directly by the typhoon.

445 Due to the observational limitations, a backward ray-tracing theory was used to
446 connect GWs in the upper mesosphere ~~and to~~ GWs ~~to in~~ the thermosphere at about 250
447 km. We found that the termination points of ray tracing of the thermospheric CGW
448 almost fell above the mesopause region, ~~which shows clear signs of primary CGW~~
449 ~~dissipation and/or nonlinear processes~~. Backward ray-tracing analysis and the CGWs

450 evolution process observed by the OH network suggested that the CGW observed in the
451 thermosphere did not directly originate from the typhoon but may have emerged due to
452 dissipation and/or nonlinear processes of typhoon-induced CGWs in the mesopause
453 region. Airglow network observations combined with numerical simulation to study the
454 generation of secondary wave in detail will be carried out in the future.

455

456 ***Data availability***

457 The Double Layer Airglow Network data are available at <http://159.226.22.74/>. The
458 ERA-5 reanalysis data are downloaded from the Copernicus Climate Change Service
459 Climate Data Store through [https://www.ecmwf.int/en/forecasts/datasets/
460 reanalysis-datasets/era5](https://www.ecmwf.int/en/forecasts/datasets/reanalysis-datasets/era5). The typhoon information are provided at
461 <http://agora.ex.nii.ac.jp/digital-typhoon/>. MTSAT-1R data is accessed from
462 <http://webgms.iis.u-tokyo.ac.jp/>.

463

464 ***Video supplement***

465 A video of detailed evolutions of CGWs excited by the Typhoon observed by OH airglow
466 observation network is provided (<https://doi.org/10.5446/55348>).

467

468 ***Author contributions***

469 J. X conceived the idea of the manuscript. Q. L. carried out the data analysis,
470 interpretation and manuscript preparation. H. L. L., X. L and W. Y. contributed to the data
471 interpretation and manuscript preparation. All authors discussed the results and

472 commented on the manuscript.

473

474 ***Competing interests***

475 The authors declare no competing interests.

476

477 ***Acknowledgements***

478 This work was supported by the National Science Foundation of China (41974179 and

479 41831073), ~~Pandeng Program of National Space Science Center, Chinese Academy of~~

480 ~~Sciences and~~ the Strategic Priority Research Program of Chinese Academy of Sciences

481 (XDA17010301), ~~and~~ the Informatization Plan of Chinese Academy of Sciences

482 (CAS-WX2021PY-0101), and the Project of Stable Support for Youth Team in Basic

483 Research Field, CAS (YSBR-018). The work was also supported by the Specialized

484 Research Fund for State Key Laboratories. We acknowledge the use of data from the

485 Chinese Meridian Project.

486

487 **References**

488 Azeem, I., Yue, J., Hoffmann, L., Miller, S. D., Straka, W. C., and Crowley, G.:

489 Multisensor profiling of a concentric gravity wave event propagating from the

490 troposphere to the ionosphere, *Geophys. Res. Lett.*,42, 7874–7880, 2015.

491 Becker, E., Vadas, S. L., Bossert, K., Harvey, V. L., Zülicke, C., and Hoffmann, L.: A

492 High-resolution whole atmosphere model with resolved gravity waves and specified

493 large-scale dynamics in the troposphere and stratosphere, *Journal of Geophysical*

494 Research: Atmospheres, 127, 2022.

495 Chun, H.-Y., and Kim, Y.-H.: Secondary waves generated by breaking of convective
496 gravity waves in the mesosphere and their influence in the wave momentum flux, J.
497 Geophys. Res., 113, D23107, 2008.

498 Chou, M. Y., Lin, C. C. H., Yue, J., Tsai, H. F., Sun, Y. Y., Liu, J. Y., and Chen, C. H.:
499 Concentric traveling ionosphere disturbances triggered by Super Typhoon Meranti
500 (2016), Geophys. Res. Lett., 44, 1219–1226, 2017.

501 Dong, W., Fritts, D. C., Lund, T. S., Wieland, S. A., and Zhang, S.: Self - acceleration and
502 instability of gravity wave packets: 2-dimensional packet propagation,
503 instability dynamics, and transient flow responses, Journal of Geophysical Research:
504 Atmospheres, 125, 2020.

505 Drob, D. P., Emmert, J. T., Meriwether, J. W., Makela, J. J., Doornbos, E., Conde, M., et al.
506 An update to the Horizontal Wind Model (HWM): The quiet time thermosphere, Earth
507 and Space Science, 2, 301–319, 2015.

508 Duncombe, J.: The surprising reach of Tonga's giant atmospheric waves, Eos, 103,
509 <https://doi.org/10.1029/2022EO220050>, 2022.

510 Franke, P. M. and Robinson, W. A.: Nonlinear behavior in the propagation of atmospheric
511 gravity waves, J. Atmos. Sci., 56, 3010-3027, 1999.

512 Fritts, D. C. and Alexander, M. J.: Gravity wave dynamics and effects in the middle
513 atmosphere, Rev. Geophys., 41(1), 1003, 2003.

514 Fritts, D. C., Vadas, S. L., Wan, K., and Werne J. A.: Mean and variable forcing of the

515 middle atmosphere by gravity waves, *J. Atmos. Sol. Terr. Phys.*, 68, 247–265, 2006.

516 Fritts, D. C., B. Laughman, T. S. Lund, and Snively, J. B.: Self-acceleration and instability
517 of gravity wave packets:1. Effects of temporal localization, *J. Geophys. Res. Atmos.*,
518 120, 8783–8803, 2015.

519 Fritts, D. C., Dong, W., Lund, T. S., Wieland, S., and Laughman, B.: Self - acceleration
520 and instability of gravity wave packets: 3.Three - dimensional packet propagation,
521 secondary gravity waves, momentum transport, and transient mean forcing in tidal
522 winds, *Journal of Geophysical Research: Atmospheres*, 125, 2020.

523 Garcia, F. J., Taylor, M. J., and Kelly, M. C.: Two - dimensional spectral analysis of
524 mesospheric airglow image data, *Applied Optics*, 36(29), 7374–7385,1997.

525 Gavrilov, N. M. and Kshevetskii, S. P.: Features of the Supersonic Gravity Wave
526 Penetration from the Earth's Surface to the Upper Atmosphere, *Radio physics and
527 Quantum Electronics*, 61(4), 243-252, 2018.

528 Heale, C. J., Snively, J. B., Bhatt, A. N., Hoffmann, L., Stephan, C. C., and Kendall, E. A.:
529 Multilayer observations and modeling of thunderstorm-generated gravity waves over
530 the Midwestern United States. *Geophysical Research Letters*, 46, 14,164–14,174.
531 <https://doi.org/10.1029/2019GL085934>, 2019.

532 Heale, C. J., Bossert, K., Vadas, S. L., Hoffmann, L., Dornbrack, A., Stober, G., et al.
533 Secondary gravity waves generated by breaking mountain waves over Europe,
534 *Journal of Geophysical Research: Atmospheres*,125, e2019JD031662, 2020.

535 Heale, C. J., Inchin, P. A., and Snively, J. B.: Primary Versus Secondary Gravity Wave

536 Responses at F-Region Heights Generated by a Convective Source, *Journal of*
537 *Geophysical Research: Space Physics*, <https://doi.org/10.1029/2021JA029947>, 2021.

538 Hersbach, H., Bell, B., Berrisford, P., Hirahara, S., Horányi, A., Muñoz-Sabater, J., Nicolas,
539 J., Peubey, C., Radu, R., Schepers, D., Simmons, A., Soci, C., Abdalla, S., Abellan, X.,
540 Balsamo, G., Bechtold, P., Biavati, G., Bidlot, J., Bonavita, M., De Chiara, G.,
541 Dahlgren, P., Dee, D., Diamantakis, M., Dragani, R., Flemming, J., Forbes, R.,
542 Fuentes, M., Geer, A., Haimberger, L., Healy, S., Hogan, R. J., Hólm, E., Janisková
543 M., Keeley, S., Laloyaux, P., Lopez, P., Lupu, C., Radnoti, G., de Rosnay, P., Rozum,
544 I., Vamborg, F., Villaume, S., and Thépaut, J. N.: The ERA5 global reanalysis, *Q. J. R.*
545 *Meteorol. Soc.*, 146(730), 1999–2049, doi:10.1002/qj.3803, 2020.

546 Hoffmann, L., Günther, G., Li, D., Stein, O., Wu, X., Griessbach, S., Heng, Y., Konopka, P.,
547 Müller, R., Vogel, B. and Wright, J. S.: From ERA-Interim to ERA5: The considerable
548 impact of ECMWF’s next-generation reanalysis on Lagrangian transport simulations,
549 *Atmos. Chem. Phys.*, 19(5), 3097–3214, doi:10.5194/acp-19-3097-2019, 2019.

550 Holton, J.R.: The influence of gravity wave breaking on the general circulation of the
551 middle atmosphere, *J. Atmos. Sci.*, 40, 2497–2507, 1983.

552 Kogure, M., Yue, J., Nakamura, T., Hoffmann, L., Vadas, S. L., Tomikawa, Y., Ejiri, M. K.,
553 and Janches, D.: First direct observational evidence for secondary gravity waves
554 generated by mountain waves over the Andes. *Geophysical Research Letters*, 47,
555 2020.

556 Kim, S.-Y., Chun, H.-Y., and Wu, D. L.: A study on stratospheric gravity waves generated
557 by Typhoon Ewiniar: Numerical simulations and satellite observations, *J. Geophys.*

558 Res., 114, D22104, 2009.

559 Li, Q., Xu, J., Yue, J., Yuan, W., and Liu, X.: Statistical characteristics of gravity wave
560 activities observed by an OH airglow imager at Xinglong, in northern China, *Annales*
561 *Geophysicae*, 29 (8), 1401–1410, 2011.

562 [Lighthill, J.: Waves in Fluids, 504 pp., Cambridge Univ. Press, New York, 1978.](#)

563 Liu, H.-L. and Vadas, S. L.: Large-scale ionospheric disturbances due to the dissipation of
564 convectively-generated gravity waves over Brazil, *J. Geophys. Res. Sp. Phys.*, 118(5),
565 2419–2427, doi:10.1002/jgra.50244, 2013.

566 Liu, H.-L., McInerney, J. M., Santos, S., Lauritzen, P. H., Taylor, M. A., and Pedatella, N.
567 M.: Gravity waves simulated by high-resolution Whole Atmosphere Community
568 Climate Model, *Geophys. Res. Lett.*, 41, 9106–9112, 2014.

569 Liu, H., Ding, F., Yue, X., Zhao, B., Song, Q., Wan, W., Ning, B., Zhang, K.: Depletion and
570 traveling ionospheric disturbances generated by two launches of China’s Long March
571 4B rocket. *Journal of Geophysical Research: Space Physics*, 123, 10,319–10,330,
572 2018.

573 Lund, T. S. and Fritts, D. C.: Numerical simulation of gravity wave breaking in the lower
574 thermosphere, *J. Geophys. Res. Atmos.*, 117, D21105, 10.1029/2012jd017536, 2012.

575 Lund, T. S., Fritts, D. C., Wan, K., Laughman, B., and Liu, H.-L.: Numerical Simulation of
576 Mountain Waves over the Southern Andes. Part I: Mountain Wave and Secondary
577 Wave Character, Evolutions, and Breaking, *Journal of the Atmospheric*
578 *Sciences*, 77(12), 4337-4356, 2020.

579 Pfeffer, R. L. and Zarichny, J.: Acoustic-Gravity Wave Propagation from Nuclear
580 Explosions in the Earth's Atmosphere, *J. Atmos. Sci.* 19, 256–263, 1962.

581 Picone, J. M., Hedin, A. E., Drob, D. P., and Aikin, A. C. NRLMSISE - 00 empirical
582 model of the atmosphere: Statistical comparisons and scientific issues, *Journal of*
583 *Geophysical Research*,107(A12), 1468, 2002.

584 Pierce, A.D., J. W. Posey, and Iliff, E. F.: Variation of nuclear explosion generated
585 acoustic-gravity wave forms with burst height and with energy yield, *J. Geophys. Res.*,
586 76, 5025-5042, 1971.

587 Sentman, D. D., Wescott, E. M., Picard, R. H., Winick, J. R., Stenbaek-Nielsen, H. C.,
588 Dewan, E. M., Moudry, D. R., Sao Sabbas, F. T., Heavner, M. J., and Morrill, J.:
589 Simultaneous observations of mesospheric gravity waves and sprites generated by a
590 midwestern thunderstorm, *J. Atmos. Sol. Terr. Phys.*, 65, 537–550, 2003.

591 Smith, S. M., Vadas, S. L., Baggaley, W. J., Hernandez, G., and Baumgardner, J.: Gravity
592 wave coupling between the mesosphere and thermosphere over New Zealand, *Journal*
593 *of Geophysical Research: SpacePhysics*,118, 2694–2707, 2013.

594 Smith, S. M., Setvák, M., Beletsky, Y., Baumgardner, J., and Mendillo, M.: Mesospheric
595 gravity wave momentum flux associated with a large thunderstorm complex, *Journal*
596 *of Geophysical Research: Atmospheres*,125, e2020JD033381, 2020.

597 Snively, J. B.: Nonlinear gravity wave forcing as a source of acoustic waves in the
598 mesosphere, thermosphere, and ionosphere, *Geophysical Research Letters*, 44,
599 12,020–12,027, 2017.

600 Suzuki, S., Shiokawa, K., Otsuka, Y., Ogawa, T., Nakamura, K., and Nakamura, T.: A
601 concentric gravity wave structure in the mesospheric airglow images, *J. Geophys.*
602 *Res.*,112, D02102, 2007.

603 Suzuki, S., Vadas, S. L., Shiokawa, K., Otsuka, Y., Kawamura, S., and Murayama, Y.:
604 Typhoon-induced concentric airglow structures in the mesopause region, *Geophys.*
605 *Res. Lett.*, 40, 5983–5987, 2013.

606 Taylor, M. J. and Hapgood, M. A.: Identification of a thunderstorm as a source of short
607 period gravity waves in the upper atmospheric nightglow emissions, *Planet. Space*
608 *Sci.*, 36, 975–985, 1988.

609 Vadas, S. L., Fritts, D. C., and Alexander, M. J.: Mechanism for the generation of
610 secondary waves in wave breaking regions, *Journal of the Atmospheric Sciences*, 60,
611 194–214, 2003.

612 Vadas, S. L., and Fritts, D. C.: Gravity wave radiation and mean responses to local body
613 forces in the atmosphere, *Journal of the Atmospheric Sciences*, 58, 2249–2279, 2001.

614 Vadas, S. L. and Fritts, D. C.: Thermospheric responses to gravity waves: Influences of
615 increasing viscosity and thermal diffusivity, *J. Geophys. Res.*, 110, D15103,
616 doi:10.1029/2004JD005574, 2005

617 Vadas, S. L.: Horizontal and vertical propagation and dissipation of gravity waves in the
618 thermosphere from lower atmospheric and thermospheric sources, *Journal of*
619 *Geophysical Research*,112, A06305, 2007.

620 Vadas, S. L., Yue, J., She, C. Y., Stamus, P., and Liu, A. Z.: A model study of the
621 effects of winds on concentric rings of gravity waves from a convective plume near
622 Fort Collins on 11 May 2004, *J. Geophys. Res.*, 114, 2009.

623 Vadas, S. L. and Crowley, G.: Sources of the traveling ionospheric disturbances observed
624 by the ionospheric TIDDBIT sounder near Wallops Island on 30 October 2007,
625 *Journal of Geophysical Research*, 115, A07324, 2010.

626 Vadas, S., Yue, J., and Nakamura, T.: Mesospheric concentric gravity waves generated by
627 multiple convective storms over the North American Great Plain, *J. Geophys. Res.*,
628 117, 2012.

629 Vadas, S. L. and Liu, H.-L.: Numerical modeling of the large-scale neutral and plasma
630 responses to the body forces created by the dissipation of gravity waves from 6 h of
631 deep convection in Brazil, *J. Geophys. Res. Sp. Phys.*, 118(5), 2593–2617,
632 doi:10.1002/jgra.50249, 2013.

633 Vadas, S. L., Zhao, J., Chu, X., and Becker, E. The excitation of secondary gravity waves
634 from local body forces: Theory and observation, *Journal of Geophysical Research:*
635 *Atmospheres*, 123, 9296–9325, 2018.

636 Vadas, S. L. and Becker, E.: Numerical modeling of the generation of tertiary gravity
637 waves in the mesosphere and thermosphere during strong mountain wave events over
638 the Southern Andes. *Journal of Geophysical Research: Space Physics*,
639 124, 7687–7718. <https://doi.org/10.1029/2019JA026694>, 2019.

640 Vadas, S. L. and Azeem, I.: Concentric Secondary Gravity Waves in the Thermosphere and
641 Ionosphere over the Continental United States on 25 - 26 March 2015 from Deep

642 Convection, *Journal of Geophysical Research: Space Physics*, 126, e2020JA028275,
643 2021.

644 Walterscheid, R. L. and Hecht, J. H.: A reexamination of evanescent acoustic-gravity
645 waves: Special properties and aeronomical significance, *J. Geophys. Res.*, 108(D11),
646 4340, doi:10.1029/2002JD002421, 2003.

647 Xu, J., Li, Q., Yue, J., Hoffmann, L., Straka, W. C., Wang, C., Liu, M., Yuan, W., Han, S.,
648 Miller, S.D., Sun, L., Liu, X., Liu, W., Yang, J., and Ning, B.: Concentric gravity
649 waves over northern China observed by an airglow imager network and satellites, *J.*
650 *Geophys. Res. Atmos.*, 120, 11,058–11,078, 2015.

651 Xu, J., Li, Q., Sun, L., Liu, X., Yuan, W., Wang, W., Yue, J., Zhang, S., Liu, W., Jiang, G.,
652 Wu, K., Gao, H., and Lai, C.: The Ground - Based Airglow Imager Network in
653 China: Recent Observational Results, *Geophysical Monograph Series*, 261, 365-394,
654 2021.

655 Xu, S., Yue, J., Xue, X., Vadas, S. L., Miller, S. D., Azeem, I., et al. Dynamical coupling
656 between Hurricane Matthew and the middle to upper atmosphere via gravity waves,
657 *Journal of Geophysical Research: Space Physics*, 124, 3589–3608, 2019.

658 Yue, J., Vadas, S. L., She, C. Y., Nakamura, T., Reising, S. C., Liu, H. L., Stamus, P.,
659 Krueger, D. A., Lyons, W., and Li, T.: Concentric gravity waves in the mesosphere
660 generated by deep convective plumes in the lower atmosphere near Fort Collins,
661 Colorado, *J. Geophys. Res. Atmos.*, 114(6), 1–12, doi:10.1029/2008JD011244, 2009.

662 Yue, J., Miller, S. D., Hoffmann, L., and Straka, W. C.: Stratospheric and mesospheric

663 concentric gravity waves over tropical cyclone Mahasen: Joint AIRS and VIIRS
664 satellite observations, *Journal of Atmospheric and Solar - Terrestrial Physics*,119,
665 83–90, 2014.

666 Zhou, X., Holton, J. R., and Mullendore, G. L.: Forcing of secondary waves by breaking
667 of gravity waves in the mesosphere, *J. Geophys. Res. Atmos.*,107, 2002.